The research on small-scale structures of ice particle density and electron density in the mesopause region

Ruihuan Tian [1,2], Jian Wu[2], Jinxiu Ma[3], Yonggan Liang [1,2], Hui Li [1,2], Chengxun Yuan[1, 4], Yongyuan Jiang[1] and Zhongxiang Zhou[1, 4]

[1]Department of Physics, Harbin Institute of Technology, Harbin 150001, China

[2]National Key Laboratory of Electromagnetic Environment (LEME), China Research Institute of Radio Wave Propagation, Beijing 102206, China

[3]CAS Key Laboratory of Geospace Environment and Department of Modern Physics, University of Science and Technology of China, Hefei 230026, China

[4] Center of Space Environment of Polar Regions, Harbin Institute of Technology, Harbin 150001, China

Correspondence to: Hui Li (lihui_2253@163.com) and Chengxun Yuan (yuancx@hit.edu.cn)

Abstract. The formation of ice particle density irregularities with meter scale in the mesopause region is explored in this paper by developing a growth and motion model of ice particles based on the motion equation of a variable mass object. The growth of particles by water vapor adsorption and the action of gravity and neutral drag force on particles are considered in the model. The evolution of radius, velocity, and number density of ice particles is then investigated by solving the growth and motion model numerically. For certain nucleus radius, it is found that the velocity of particles can be reversed at a particular height, leading to local gathering of particles near the boundary layer, which then form small-scale ice particle density structures. The spatial scale of the density structures can be affected by vertical wind speed, water vapor density, and altitude, and remain stable as long as these environmental parameters do not change. The influence of the stable small-scale structures on electron and ion density is further calculated by a charging model, which considers the production, loss, and transport of electrons and ions, along with dynamic particle charging processes. Results show that, the electron density is anti-correlated to the charged ice particle density and ion density for particles with radii of 11 nm or less due to plasma attachment by particles and plasma diffusion. This finding is in accordance with most rocket observations. The small-scale electron density structures created by small-scale ice particle density irregularities can produce the polar mesosphere summer echoes (PMSE) phenomenon.

1 Introduction

Polar mesosphere summer echoes (PMSE) are strong radar echoes from the polar mesopause in summer(Rapp and Lübken 2004). One of the features of PMSE is that the spectral widths of echoes are much narrower than that of incoherent scatter due to the Brownian movement of electrons(Röttger, et al. 1988; Röttger, et al. 1990). It has been proposed that PMSE are caused by radar waves cohenertly scattered by irregularities in the refractive index, which are mainly determined by electron density (Rapp and Lübken 2004). The efficient scattering occurs when the spatial scale of electron density structures is half of the radar wavelength, which is called Bragg scale. the scale is approximately 3 m for typical VHF radars (Rapp and Lübken 2004). In the ECT02 rocket campaign(Lübken, et al. 1998), a sounding rocket with electron probes detected electron density irregularities in the order of meters during a simultaneous observation of PMSE, providing a compelling argument that small-scale electron density structures can indeed create strong radar echoes.

A large amount of research indicates that small scale ice particle density irregularities in the PMSE region play a key role in creating and maintaining small-scale structures of electron density (Chen and Scales 2005;Lie‐Svendsen, et al. 2003;Mahmoudian and Scales 2013;Rapp and Lübken 2003;Scales and Ganguli 2004). Markus Rapp and Franz-Josef Lübken investigated electron diffusion in the vicinity of charged particles revisited (Rapp and Lübken 2003). They developed coupled diffusion equations for electrons, charged aerosol particles, and positive ions subject to the initial condition of anti-correlated perturbations in charged aerosol and electron distribution. The results illustrate that the perturbations of electron density are anti-correlated to that of the negatively charged aerosol particles and positive ions. Lie-Svendsen et al. studied the plasma response to imposed small-scale aerosol particle density perturbations (Lie‐Svendsen, et al. 2003). The results were consistent with the solution provided by Markus Rapp's model, in which particle density structures in the order of a few meters could lead to small-scale electron density perturbations due to electron attachment and ambipolar diffusion.

In the work mentioned above, aerosol particle density profiles were directly set as specific small scale structures such as Gaussian, hyperbolic tangent or sinusoidal. However, the formation mechanism of the small-scale particle density structures can contribute to a more comprehensive understanding of the PMSE phenomenon and is neglected in such studies. Kopnin et al. used dust acoustic solitons to explain the localized structures of the charged dust particles in the PMSE region (Kopnin, et al. 2004), but the

spatial scales of the obtained structures were much smaller than the observed scale and wavelength of VHF radar. Therefore, the formation mechanism of small scale structures in the PMSE region remains not clear.

In the polar mesopause region, neutral airflow moves upward (Garcia and Solomon 1985). The ice particles are subject to upward neutral drag force and downward gravity, and grow by absorbing water vapor simultaneously. In addition, the size of initial condensation nuclei has a certain distribution. These factors can cause complex trajectories of ice particles and result in an inhomogeneous distribution of particle number density, leading to small-scale structures of electron density. This may be an important mechanism that can produce PMSE phenomenon. However, few studies have explored the formation process of small-scale ice particle structures from the perspective of ice particle growth and movement.

A particle growth and motion model is thus developed in this paper to describe the evolution of ice particle radius, velocity and density distribution in the mesopause region. The growth of particles is based on the collision and adsorption process of condensation nuclei and water vapor. The particle movement is predominantly controlled by the gravity and the neutral drag force. With the obtained ice particle density structures, the corresponding electron and ion densities are calculated based on a charging model, which includes the continuity equations for ice particles with various charges and ions, the momentum equation for ions and electrons, and the quasi-neutral condition.

2 Model

Equations for the growth and motion model of condensation nuclei and the charging model of ice particles are detailed in this section.

The simulation is carried out at summer polar mesopause region between 80 ~ 90 km, where the water vapor carried by neutral gas is determined to move upwards at a constant speed (Garcia and Solomon 1985). It is assumed that micrometeorites enter the study region at a certain flux from the upper boundary, and volcanic ash or particles ejected by the aircraft rise into the region from the lower boundary. These grains serve as condensation cores. When the temperature is lower than the frost point (Körner and Sonnemann 2001), water vapor molecules that touch the surface of the grains due to thermal motion can easily condense into ice. In this process, condensation cores become ice particles and continue to grow. In this article, only the growth, motion, and charging process of particles inside the condensation layer are discussed, and only the vertical transport of particles and plasma is

considered as the horizontal gradients of transport parameters are much smaller comparatively (Lie - Svendsen, et al. 2003).

For growing ice particles, the dynamic equation for variable mass object is applied:

$$m_{\mathrm{d}} \frac{\mathrm{d}\boldsymbol{u}_{\mathrm{d}}}{\mathrm{d}t} + (\boldsymbol{u}_{\mathrm{d}} - \boldsymbol{u}) \frac{\mathrm{d}m_{\mathrm{d}}}{\mathrm{d}t} = m_{\mathrm{d}}\boldsymbol{g} - \mu_{\mathrm{dn}} m_{\mathrm{d}} (\boldsymbol{u}_{\mathrm{d}} - \boldsymbol{u}) + q_{\mathrm{d}}\boldsymbol{E} \tag{1}$$

where m_{d}, $\boldsymbol{u}_{\mathrm{d}}$, and q_{d} are the mass, velocity, and charge of ice particles, respectively. $\boldsymbol{u}$ is the velocity of neutral gas, $\boldsymbol{g}$ is gravitational acceleration, μ_{dn} is the collision frequency between ice particles and gas, and $\boldsymbol{E}$ is the electric field. The electric force has a trivial effect on the motion of ice particles, because the charge-mass ratio of particles is usually very small (Jensen and Thomas 1988;Pfaff, et al. 2001). The inertial term is also negligible as its magnitude is much smaller than gravity (Garcia and Solomon 1985).

The water vapor is supersaturated in the polar mesopause region (Lübken 1999) and it is assumed that the size of condensation nuclei is larger than the condensation critical size, so stable growth of ice particles will continue when water molecules collide with particles during thermal motion. Ignoring reverse processes such as sublimation, the mass change rate of ice particles is

$$\frac{\mathrm{d}m_{\mathrm{d}}}{\mathrm{d}t} = \mu_{\mathrm{wd}} m_{\mathrm{w}} \tag{2}$$

The collision frequency between water vapor and ice particles is $\mu_{\mathrm{wd}} = n_{\mathrm{w}} \pi r_{\mathrm{d}}^2 v_{\mathrm{w}}$ based on the hard-sphere collision model (Lieberman and Lichtenberg 2005), in which m_{w}, n_{w} and v_{w} are the mass, number density, and thermal velocity of water molecules, respectively.

The collision frequency between air molecules and ice particles in the neutral drag force term is(Schunk 1977)

$$\mu_{\mathrm{dn}} = \frac{8}{3\sqrt{\pi}} \frac{n_{\mathrm{n}} m_{\mathrm{n}}}{m_{\mathrm{d}} + m_{\mathrm{n}}} \sqrt{\frac{2k_{\mathrm{B}} T_{\mathrm{g}} (m_{\mathrm{d}} + m_{\mathrm{n}})}{m_{\mathrm{d}} m_{\mathrm{n}}}} \pi (r_{\mathrm{d}} + r_{\mathrm{n}})^2 \tag{3}$$

where n_{n}, m_{n}, and r_{n} are number density, mean molecule mass, and effective radius of neutral molecule, respectively, and T_{g} is the gas temperature. The neutral molecule mass m_{n} is assumed to be $28.96 m_{\mathrm{u}}$, in which $\mathrm{m_u}$ is the proton mass.

According to Eq. (1) the velocity of ice particles is obtained as

$$\boldsymbol{u}_{\mathrm{d}} = \boldsymbol{u} + \frac{m_{\mathrm{d}}}{\mu_{\mathrm{dn}} m_{\mathrm{d}} + \mu_{\mathrm{wd}} m_{\mathrm{w}}} \boldsymbol{g} \tag{4}$$

On the basis that $n_w << n_n$(Seele and Hartogh 1999), $m_w << m_d$, $m_n << m_d$, $r_n << r_d$, $v_n \sim v_w$, and taking vertical up to be the positive direction, the velocity of ice particles is simplified as

$$u_d = u - g/\mu_{dn} \tag{5}$$

Ice particles are composed of condensation nuclei and the attached ice. The mass of a single ice particle is

$$m_d = \frac{4}{3}\pi r_0^3 \rho_0 + \frac{4}{3}\pi(r_d^3 - r_0^3)\rho_d \tag{6}$$

where r_0 and ρ_0 are the initial radius and mass density of condensation nuclei, and ρ_d is the mass density of ice.

Based on the expressions of m_d and μ_{dn}, the relation between ice particle velocity and radius is

$$u_d = u - \frac{g}{n_n m_n v_n}[\rho_d r_d + (\rho_0 - \rho_d)\frac{r_0^3}{r_d^2}] \tag{7}$$

At the boundaries of the condensation region $r_d = r_0$, and the initial velocity of condensation nuclei is

$$u_{d0} = u(1 - r_0/r_c) \tag{8}$$

where r_c is the critical radius

$$r_c = n_n m_n v_n u/(g\rho_0) \tag{9}$$

When the radius of condensation nuclei $r_0 > r_c$, gravity is larger than the neutral drag force, $v_{d0} < 0$, and particles move downwards. Otherwise, particles move upwards.

Based on the relation between m_d and r_d, the change rate of ice particle radius is

$$\frac{dr_d}{dt} = \frac{1}{4}\frac{n_w m_w v_w}{\rho_d} = c \tag{10}$$

It can be clearly observed that the ice particle radius increases linearly with time:

$$r_d = r_0 + ct \tag{11}$$

The particle trajectory can then be obtained by the following integral

$$z - z_0 = \int_0^t u_d dt = c^{-1}\int_{r_0}^{r_d} u_d dr_d \tag{12}$$

where z_0 is the reference height where condensation nuclei enter the studied region. In this work $z_0 = 0$

is set at the lower boundary and $z_0 = h$ is set at the upper boundary, where h is the distance between the two boundaries.

It is assumed that the condensation nucleus radius ranging from $r_{0\min}$ to $r_{0\max}$ has a certain distribution function $f(r_0)$. The density of condensation nuclei with radius in the small range $r_0 \rightarrow r_0 + \mathrm{d}r_0$ is $\mathrm{d}n(r_0) = f(r_0)\mathrm{d}r_0$, and their velocity is $u_{\mathrm{d}0}$. When these particles arrive at height z, their radius increases to $r_{\mathrm{d}}(r_0, z)$, the corresponding number density turns into $\mathrm{d}n(r_0, z)$, and the velocity becomes $u_{\mathrm{d}}(r_0, z) = u_{\mathrm{d}}[r_0, r_{\mathrm{d}}(r_0, z)]$. According to the particle-conservation law

$$u_{\mathrm{d}0}\mathrm{d}n(r_0) = u_{\mathrm{d}}(r_0, z)\mathrm{d}n(r_0, \mathrm{z}) \tag{13}$$

The number density of ice particles at height z can then be obtained by

$$n_{\mathrm{d}}(z) = \int \mathrm{d}n(r_0, z) = \int_{r_{0\min}}^{r_{0\max}} \frac{u_{\mathrm{d}0} f(r_0)}{u_{\mathrm{d}}(r_0, z)} \mathrm{d}r_0 \tag{14}$$

The averaged ice particle radius at height z is

$$\overline{r}_{\mathrm{d}}(z) = \frac{\int r_{\mathrm{d}}(z)\mathrm{d}n(r_0, z)}{n_{\mathrm{d}}(z)} \tag{15}$$

By integrating all condensation nucleus radii, a stable distribution of n_{d} and r_{d} can be obtained. The particles continue to enter and leave the condensation region, and as long as the external environment does not change, the distribution of particle density and radius will remain unchanged. The influence of these stable n_{d} and r_{d} profiles on electron and ion density is then calculated.

Considering ionization, electron-ion recombination, and ion loss on ice particles, the continuity equation of ion density can be written as

$$\frac{\partial n_{\mathrm{i}}}{\partial t} + \frac{\partial (n_{\mathrm{i}} u_{\mathrm{i}})}{\partial z} = Q - \alpha n_{\mathrm{i}} n_{\mathrm{e}} - D^{+} n_{\mathrm{i}} \tag{16}$$

Ignoring gravity, the drift velocity of ions u_{i} is determined by

$$u_{\mathrm{i}} = \frac{eE}{m_{\mathrm{i}}\mu_{\mathrm{in}}} - \frac{k_{\mathrm{B}}T_{\mathrm{g}}}{m_{\mathrm{i}}\mu_{\mathrm{in}}} \frac{1}{n_{\mathrm{i}}} \frac{\partial n_{\mathrm{i}}}{\partial z} \tag{17}$$

The electric field E is predominantly determined by electron density gradient because the diffusion coefficient and mobility of electrons are much larger than that of ions:

$$E = -\frac{k_{\mathrm{B}}T_{\mathrm{g}}}{e} \frac{1}{n_{\mathrm{e}}} \frac{\partial n_{\mathrm{e}}}{\partial z} \tag{18}$$

In the typical PMSE layer, there are several kinds of ions carrying one unit positive charge: N_2^+, O_2^+, NO^+, and $H^+(H_2O)_n$. As specified by Reid (Reid 1990), the averaged ion parameters n_i, m_i, and T_g are applied to describe the density, mass, and temperature of ions, respectively, and the averaged ion mass m_i is set as $50m_u$ at 85 km altitude. According to Hill and Bowhill's theory (Hill and Bowhill 1977), the ion-neutral collision frequency is

$$\mu_{in} = 2.6\times10^{-15} n_n \left(0.78\frac{28}{M_i+28}\sqrt{1.74\frac{M_i+28}{28M_i}} + 0.21\frac{32}{M_i+32}\sqrt{1.57\frac{M_i+32}{32M_i}} + 0.01\frac{40}{M_i+40}\sqrt{1.64\frac{M_i+40}{40M_i}} \right) \tag{19}$$

where $M_i = m_i/m_u$.

The production rate for ions and electrons Q is chosen as 3.6×10^7 $m^{-3}s^{-1}$ and electron-ion recombination coefficient α is set as 10^{-12} m^3s^{-1} (Lie - Svendsen, et al. 2003). The undisturbed density of ions and electrons is $n_0 = 6 \times 10^9$ m^{-3}. The loss coefficient of ions on ice particles is $D^+ = \Sigma n_q v_{i,q}$, where n_q is the number density of the q-charged ice particles, and $v_{i,q}$ represents the capture rate of ions by ice particles with q charges. According to the discrete charging model (Robertson and Sternovsky 2008):

$$v_{i,q\le0} = \pi r_d^{\,2} c_i \left(1 + C_q\sqrt{\frac{e^2}{16\varepsilon_0 k_B T_g r_d}} + D_q\frac{e^2}{4\pi\varepsilon_0 k_B T_g r_d} \right) \tag{20}$$

The particle radius r_d used here is the averaged radius $\bar{r}_d$, which is obtained using Eq. (15). The ion thermal velocity $c_i = (8k_BT_g/\pi m_i)$, k_B is Boltzmann's constant, and ε_0 is the permittivity of vacuum. The C_q and D_q are provided in Table 1 of Robertson and Sternovsky's work (Robertson and Sternovsky 2008), and the corresponding capture rates of electrons by ice particles (Robertson and Sternovsky 2008) are denoted as

$$v_{e,q\ge0} = \pi r_d^{\,2} c_e \left(1 + C_q\sqrt{\frac{e^2}{16\varepsilon_0 k_B T_g r_d}} + D_q\frac{e^2}{4\pi\varepsilon_0 k_B T_g r_d} \right) \tag{21}$$

$$v_{e,q<0} = \pi r_d^{\,2}\gamma^2 c_e \exp\left[-\frac{|q|e^2}{4\pi\varepsilon_0 k_B T_g r_d \gamma}\left(1 - \frac{1}{2\gamma\left(\gamma^2-1\right)|q|} \right) \right] \tag{22}$$

The thermal velocity of electrons $c_e = (8k_BT_g/\pi m_e)$, and the value of γ for each q is referred from

Natanson's paper (Natanson 1960).

Although the distribution of total particle density $n_d = \Sigma n_q$ reaches stable state under the action of gravity and neutral drag force, the number density of the q-charged ice particles n_q is dynamic in the charging process. The continuity equation of q-charged ice particle density is

$$\frac{\partial n_q}{\partial t} = n_{q+1}\nu_{e,q+1}n_e + n_{q-1}\nu_{i,q-1}n_i - (n_q\nu_{e,q}n_e + n_q\nu_{i,q}n_i) \tag{23}$$

According to previous research (Lie - Svendsen, et al. 2003;Rapp and Lübken 2001), it is assumed that a single particle carries two negative charges at the most, i.e., q = -2, -1, 0, and +1 in this study.

According to typical parameters in the PMSE region (Rapp and Lübken 2001), the plasma Debye length λ_D is estimated to be approximately 9 mm, which is much smaller than the vertical spatial scale of the PMSE layer. Thus, the dusty plasma satisfies the quasi-neutral condition:

$$n_i + \sum_q q n_q = n_e \tag{24}$$

For simplicity, dimensionless parameters will be used in subsequent discussion:

$$V_d = v_d/u,\quad \rho = \rho_d/\rho_0,\quad R_0 = r_0/r_c,\quad R_d = r_d/r_c$$
$$T = t/t_c,\quad Z = (z - z_0)/z_c$$

where $t_c = r_c/c$, which represents the time it takes for ice particles to grow from r_d to $r_d + r_c$, and $z_c = ut_c$ is the distance that neutral wind moves during the time t_c.

The expression of dimensionless ice particle velocity is

$$V_d = 1 - \rho R_d - (1-\rho)\frac{R_0^3}{R_d^2} \tag{25}$$

The expressions of dimensionless position coordinate of particles based on T and R_d are

$$Z(R_0, T) = T - \frac{1}{2}\rho T(T + 2R_0) - (1-\rho)R_0^2\frac{T}{T + R_0} \tag{26}$$

$$Z(R_0, R_d) = R_d - R_0 - \frac{1}{2}\rho(R_d^2 - R_0^2) + (1-\rho)R_0^3\left(\frac{1}{R_d} - \frac{1}{R_0}\right) \tag{27}$$

The dimensionless number density and radius distribution of ice particles are

$$n_d(Z) = n_0\int_{R_{0min}}^{R_{0max}} \frac{V_{d0}F(R_0)}{V_d[R_0, R_d(R_0, Z)]}dR_0 \tag{28}$$

$$\bar{R}_{\mathrm{d}}(Z) = \frac{n_0}{n_{\mathrm{d}}(Z)} \int_{R_{0\min}}^{R_{0\max}} \frac{R_{\mathrm{d}}(Z) V_{\mathrm{d}0} F(R_0)}{V_{\mathrm{d}}[R_0, R_{\mathrm{d}}(R_0, Z)]} \mathrm{d}R_0 \quad (29)$$

where n_0 is the density of condensation cores at the boundary, and is assumed to be 5×10^8 m^{-3} (Bardeen, et al. 2008). The normalized radius distribution function $F(R_0)$ satisfies $\int_{R_{0\min}}^{R_{0\max}} F(R_0)\mathrm{d}R_0 = 1$.

In subsequent calculations, parameters are taken in the atmospheric environment at an altitude of 85 km. The number density of neutrals $n_{\mathrm{n}} = 2.3\times10^{20}$ m^{-3}(Hill, et al. 1999), the number density of water vapor $n_{\mathrm{w}} = 2.5\times10^{14}$ m^{-3}(Seele and Hartogh 1999), temperature $T_{\mathrm{g}} = 150$ K, the mass density of ice $\rho_{\mathrm{d}} = 1\times10^3$ kg/m^3, the velocity of neutral wind $u = 3$ cm/s(Garcia and Solomon 1985), the mass density of condensation nucleus $\rho_0 = 2.7\times10^3$ kg/m^3, and the growth rate of ice particles $c \approx 7.8\times10^{-4}$ nm/s. In this work, we only consider the growth and movement of condensation nuclei which fall from the upper boundary with initial radius $r_0 > r_{\mathrm{c}}$ and rise from lower boundary with $r_0 \leq r_{\mathrm{c}}$.

3 Results and Discussion

3.1 Speed and trajectory of ice particles

The relation between V_{d} and R_{d} is illustrated in Fig. 1(a), which shows that condensation nuclei with initial radius $R_0 \leq 1$ rise into the PMSE region through the lower boundary, while particles with $R_0 > 1$ fall into the region from the upper boundary. At the beginning, the upward-moving particles accelerate and the downward particles decelerate due to $\partial V_{\mathrm{d}}/\partial R_{\mathrm{d}} = 2 - 3\rho > 0$ when $R_{\mathrm{d}} = R_0$. Later, with the increase of R_{d}, $\partial V_{\mathrm{d}}/\partial R_{\mathrm{d}} < 0$, all particles will move with a downward acceleration, which makes them move downward eventually.

Figure 1(b) shows the movement curves of ice particles near the lower boundary. These particles, with an initial radius $R_0 \leq 1$ will rise into the condensation layer. With the collection of ice, the grains become larger and heavier, leading to their deceleration. The grains will then accelerate downward until they leave the condensation layer from the lower boundary. All particles rising from the lower boundary will retrace in the range $Z_{\mathrm{m}} < Z < Z_{\mathrm{M}}$. Z_{m} is the maximum height that particles with initial radius $R_0 = 1$ can reach and Z_{M} is the maximum height that particles with initial radius $R_0 = R_{0\min} = 0.5$ can reach. Based on above parameters, $Z_{\mathrm{m}} = 0.1512$ and $Z_{\mathrm{M}} = 0.7682$.

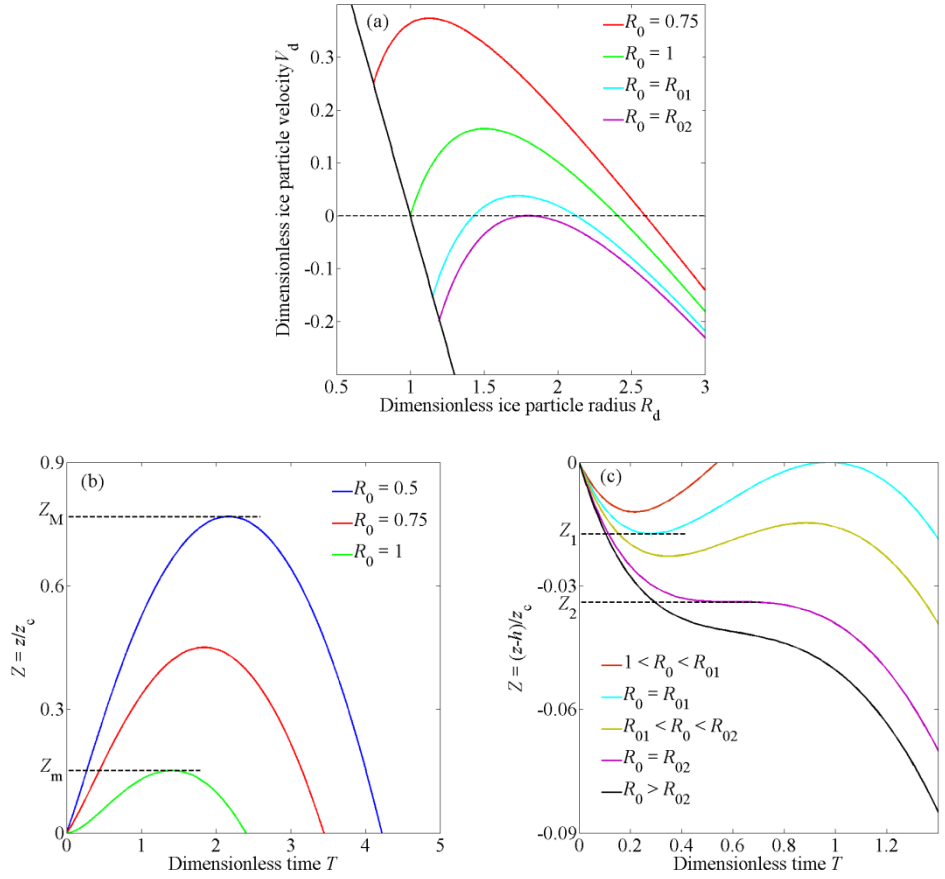

Figure 1 (a) Dependence of the ice particle velocity on radius for different initial nucleus radii. The black solid line $V_{d0} = 1 - R_0$ represents the relation between the initial particle velocity and the initial particle radius; (b) Movement curves of ice particles near the lower boundary; (c) Movement curves of ice particles near the upper boundary.

Figure 1(c) shows the movement curves of ice particles near the upper boundary, which can be sorted by the value of R_0. For $1 < R_0 < R_{01}$, the neutral drag force increases faster than gravity as the particles fall. The particles decelerate to zero speed, retrace upward, and then leave the condensation layer from the upper boundary. For $R_0 = R_{01}$, the particles retrace at the height $Z = Z_1$, then they arrive at $Z = 0$ with exactly zero velocity, and the particles move back into the condensation layer again. For $R_{01} < R_0 < R_{02}$, the particles retrace upward in the range of $Z_2 < Z < Z_1$ and move downward again before they reach the upper boundary. For $R_0 = R_{02}$, the particles decelerate downward until zero speed at $Z = Z_2$. Here, the acceleration happens to be zero. Then the gravity exceeds the drag force, and the particles accelerate

downward. For $R_0 > R_{02}$, the particles continue moving down after entering the condensation layer. According to above parameters, R_{01} and R_{02} are solved as 1.1519 and 1.19705, respectively.

It can be observed in Fig. 1 that the particles with certain initial radius will move up and down several times near the boundary, namely, ice particles will accumulate at that region and form some kind of small-scale density structure.

3.2 Density and radius distribution of ice particles and their effects on plasma

3.2.1 Near the lower boundary

The density and radius distribution of ice particles near the lower boundary are first solved. As illustrated in Fig. 1(b), all ice particles with initial radius $R_0 \leq 1$ will pass the range $0 < Z < Z_m$ twice, so they contribute twice to the calculation of particle density. In the height range $Z_m < Z < Z_M$, only the particles that can reach the Z height will contribute to the density at Z. The density and mean radius of ice particles near the lower boundary are shown below:

$$n_d(Z) = n_0 \int_{0.5}^{R_{0Z}} V_{d0} F(R_0) \left[\frac{1}{V_{d1}(R_0, R_{d1})} + \frac{1}{|V_{d2}(R_0, R_{d2})|} \right] dR_0 \tag{30}$$

$$\bar{R}_d(Z) = \frac{n_0}{n_d(Z)} \int_{0.5}^{R_{0Z}} V_{d0} F(R_0) \left[\frac{R_{d1}}{V_{d1}(R_0, R_{d1})} + \frac{R_{d2}}{|V_{d2}(R_0, R_{d2})|} \right] dR_0 \tag{31}$$

where R_{d1} and R_{d2} are particle radii when particles pass through the Z height, V_{d1} and V_{d2} are the corresponding velocities, and the upper limit of integral R_{0Z} is determined by

$$R_{0Z} = \begin{cases} 1 & \text{if } 0 < Z < Z_m \\ \text{solution of } \left(Z\left(R_{0Z}, R_d\right) = Z \right) & \text{if } Z_m < Z < Z_M \end{cases} \tag{32}$$

In this study, the radius distribution function of condensation cores is assumed as Gaussian distribution

$$F(R_0) = A \exp[-(R_0 - R_{00})^2 / \Delta^2] \tag{33}$$

where the center of the radius distribution function R_{00} is chosen as 0.8, the characteristic width Δ = 0.01, and the corresponding normalized coefficient A = 56.4.

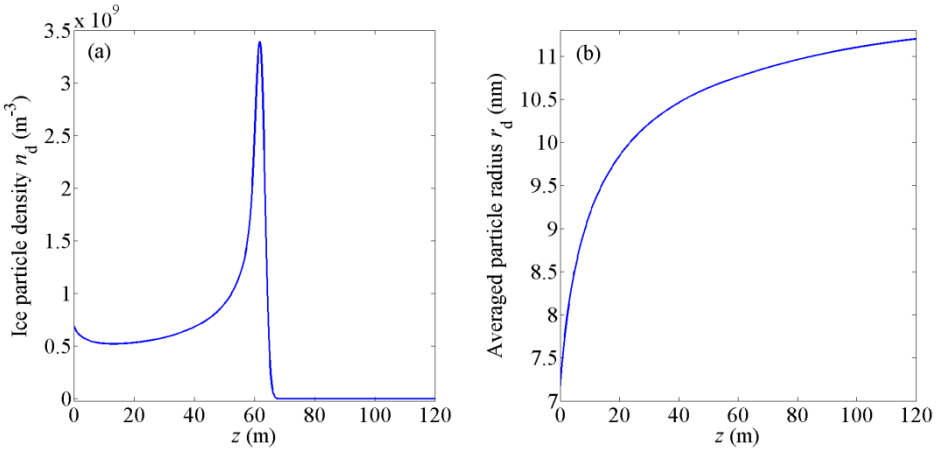

Figure 2 Distribution of (a) ice particle density and (b) averaged particle radius near the lower boundary of the condensation layer.

The obtained density and mean radius of ice particles near the lower boundary are presented in Fig. 2(a) and (b), respectively. Figure 2(a) shows that a sharp peak appears in the density distribution of ice particles. The width at half maximum of the irregularity is about 5 m, which is consistent with the assumed ice particle density structure scale in the theoretical work (Lie-Svendsen, et al. 2003;Rapp and Lübken 2003) as well as observation by the sounding rocket flight ECT02 in July 1994 (Rapp and Lübken 2004). In Fig. 2(b), it can be observed that the average radius of ice particles increases from 7 nm to 11 nm with height.

According to the obtained density and average radius of ice particles in Fig. 2(a) and (b), the density distribution of electrons, ions, and charged ice particles is calculated based on the charging model described by Eq. (16) ~ (24). At the initial moment of the charging model, all ice particles are assumed to be neutral in order to conduct the calculation more conveniently, as the final distributions of charge are independent from the initial ice particle charge state (Lie‐Svendsen, et al. 2003). The timescale of electrons collected by negatively charged particles with a radius of 10 nm is approximately 700 s, which is the longest timescale in the charging process. The quasi-steady state of charging can then be obtained after this timescale. Therefore, the calculation is terminated after 1000 s and the results are illustrated in Fig. 3.

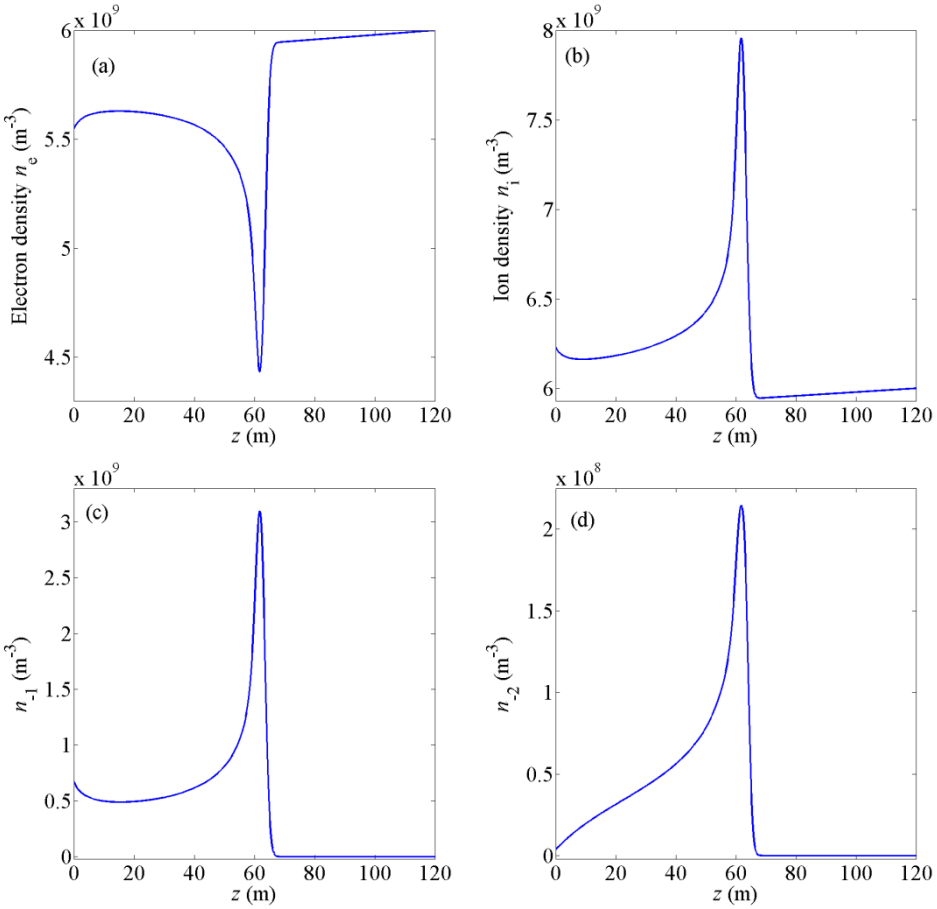

Figure 3 Number density distribution of (a) electrons n_e, (b) ions n_i, (c) particles carrying one negative charge n_{-1}, and (d) particles carrying two negative charges n_{-2} near the lower boundary of condensation layer at t = 1000 s.

Figure 3(a) shows that electron density decreases sharply around z = 60 m due to adsorption by particles and the reduction of electron density $\Delta n_e \approx (n_{-1} + 2n_{-2})/2$, which corresponds to the results under diffusion equilibrium approximations in earlier work (Lie‐Svendsen, et al. 2003). Ion number density increases sharply around 60 m due to diffusion under the ambipolar electric field. The ambipolar diffusion process of electrons and ions has been described in detail in previous work (Lie‐Svendsen, et al. 2003). Electron density is anti-correlated to density irregularities of ions and the charged ice particles due to the attachment and diffusion processes. The anti-correlations correspond with rocket observations by sounding rocket flight SCT-06 in August 1993 (Lie‐Svendsen, et al. 2003) and sounding rocket flight ECT02 in July 1994 (Rapp and Lübken 2004). According to Fig. 3(c) and (d), it can be

determined that for particles with radii ranging from 7 nm to 11 nm, the proportion of particles carrying one negative charge ranges from 97.5% to 85.1%, and the value for particles carrying two negative charges is 0.53% - 13.6%, which is consistent with observations by Havnes et al. (Havnes, et al. 1996) and numerical results by Rapp and Lübken (Rapp and Lübken 2001). The density of positively charged particles is less than 1.1×10^5 m^{-3} and is insignificant in this study.

3.2.2 Near the upper boundary

The parameters of ice particles and plasma near the upper boundary are discussed in this subsection, based on the movement curves of ice particles near the upper boundary, as shown below:

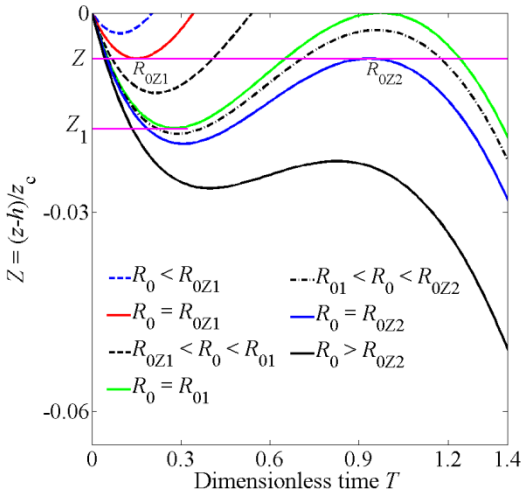

Figure 4 Movement curves of ice particles near the upper boundary. The particles with initial radius R_{0Z1} move upward after turning back at the Z height (the red line), and the particles with initial radius R_{0Z2} move downward after turning back at Z (the blue line).

For $Z_1 < Z < 0$, particles with initial radius R_{0Z1} and R_{0Z2} turn back at Z and move upward and downward separately, as shown in Fig. 4. The values of R_{0Z1} and R_{0Z2} are determined by equations $V_d(R_{0Z}, R_d) = 0$ and $Z(R_{0Z}, R_d) = Z$. The contribution of ice particles to the density distribution near the upper boundary can be classified as follows:

(1) $R_0 < R_{0Z1}$: Ice particles cannot reach Z and make no contributions to the number density;

(2) $R_{0Z1} < R_0 < R_{01}$: Ice particles pass through Z twice and contribute to $n_d(Z)$ twice. The radius of particles when passing through Z height can be obtained as R_{d31} and R_{d32} based on Eq. (27). Their

corresponding velocities are calculated respectively as V_{d31} and V_{d32} based on Eq. (25);

(3) $R_{01} < R_0 < R_{0Z2}$: Ice particles pass through Z three times. The corresponding radii and velocities at Z are defined as R_{d41}, R_{d42}, R_{d43}, and V_{d41}, V_{d42}, V_{d43};

(4) $R_0 > R_{0Z2}$: Ice particles pass through Z only once and their radius and velocity are R_{d5} and V_{d5}, respectively.

Substituting these parameters into Eq. (28) and (29), the density and mean radius of ice particles in the range $Z_1 < Z < 0$ are deduced as

$$\begin{aligned} n_d(Z) = {} & n_0 \int_{R_{0Z1}}^{R_{01}} |V_{d0}| F(R_0) \left[\frac{1}{|V_{d31}(R_0, R_{d31})|} + \frac{1}{V_{d32}(R_0, R_{d32})} \right] dR_0 \\ & + n_0 \int_{R_{01}}^{R_{0Z2}} |V_{d0}| F(R_0) \left[\frac{1}{|V_{d41}(R_0, R_{d41})|} + \frac{1}{V_{d42}(R_0, R_{d42})} + \frac{1}{|V_{d43}(R_0, R_{d43})|} \right] dR_0 \\ & + n_0 \int_{R_{0Z2}}^{R_{0max}} \frac{|V_{d0}| F(R_0)}{|V_{d5}(R_0, R_{d5})|} dR_0 \end{aligned} \quad (34)$$

$$\begin{aligned} \bar{R}_d(Z) = {} & \frac{n_0}{n_d(Z)} \int_{R_{0Z1}}^{R_{01}} |V_{d0}| F(R_0) \left[\frac{R_{d31}}{|V_{d31}(R_0, R_{d31})|} + \frac{R_{d32}}{V_{d32}(R_0, R_{d32})} \right] dR_0 \\ & + \frac{n_0}{n_d(Z)} \int_{R_{01}}^{R_{0Z2}} |V_{d0}| F(R_0) \left[\frac{R_{d41}}{|V_{d41}(R_0, R_{d41})|} + \frac{R_{d42}}{V_{d42}(R_0, R_{d42})} + \frac{R_{d43}}{|V_{d43}(R_0, R_{d43})|} \right] dR_0 \\ & + \frac{n_0}{n_d(Z)} \int_{R_{0Z2}}^{R_{0max}} \frac{R_{d5} |V_{d0}| F(R_0)}{|V_{d5}(R_0, R_{d5})|} dR_0 \end{aligned} \quad (35)$$

The center of the radius distribution function R_{00} = 1.08, the characteristic width Δ = 0.01, and the corresponding normalized coefficient A = 56.4.

The ice particle density in the region of $Z < Z_1$ is close to zero, as only particles with initial radius $R_0 \geq R_{01}$ can arrive at the region and the number of the particles in this radius range is very low based on the radius distribution function set above.

At the upper boundary, the number density of condensation cores n_0 is set as 5×10^8 m^{-3} and the maximum radius of condensation cores R_{0max} = 1.3. The number density and mean radius of ice particles are obtained from Eq. (34) and (35) and are shown in Fig. 5. The density distribution of electrons, ions, and charged ice particles is then calculated further based on the charging model.

Figure 5(a) shows that there is a meter scale structure in the distribution of ice particle density, which is consistent with the assumed ice particle density structure scale in previous theoretical work (Lie - Svendsen, et al. 2003; Rapp and Lübken 2003) and rocket observations (Rapp and Lübken 2004). In

addition, the average radius of ice particles is slightly larger than 5 nm (shown in Fig. 5(b)).

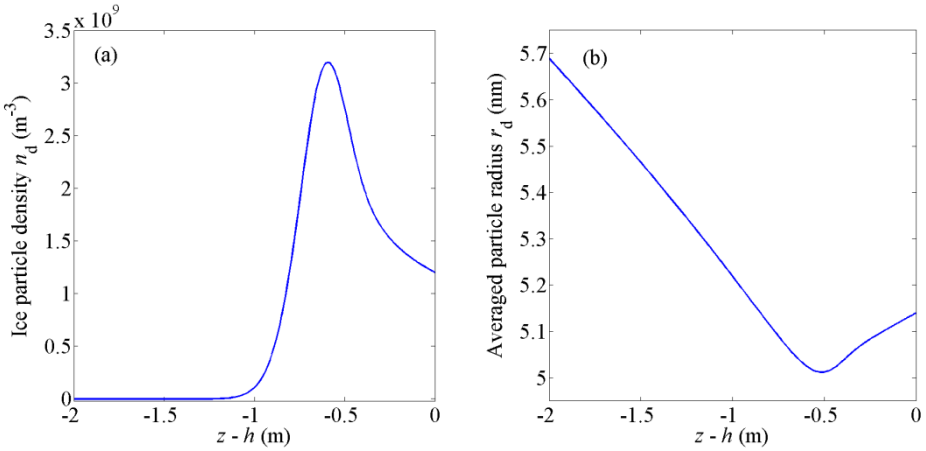

Figure 5 The distribution of (a) ice particle density and (b) the averaged particle radius near the upper boundary of condensation layer.

As illustrated in Fig. 6(a), compared with ice particle density, there is a similar but anti-correlated structure in electron density profile because of the adsorption of electrons by particles. Due to ambipolar diffusion, ion density increases in the perturbed region. The reduction of electron density Δn_e and the increment of ion density Δn_i are consistent with the results under diffusion equilibrium approximations: $\Delta n_e \approx \Delta n_i \approx (n_{-1} + 2n_{-2})/2$ (Lie‐Svendsen, et al. 2003). According to Fig. 6(c) and (d), 97% of the particles carry one negative charge, and few particles carry two negative charges. This is reasonable for particles with radius slightly larger than 5 nm.

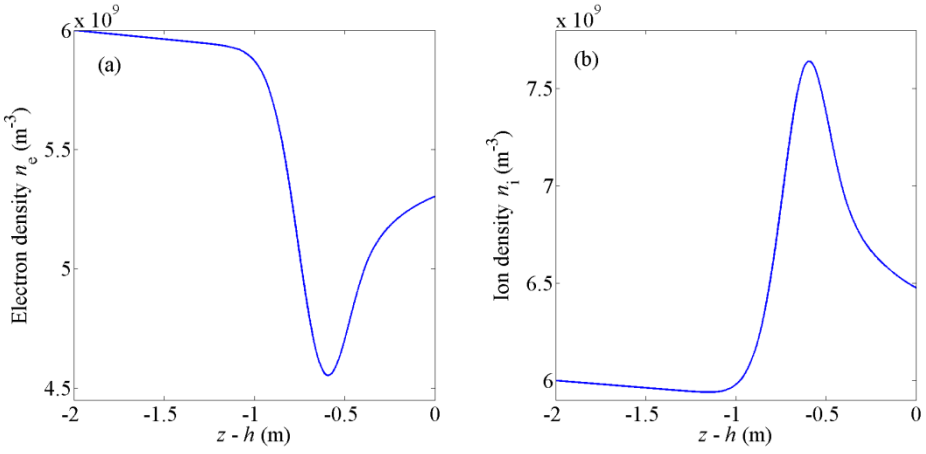

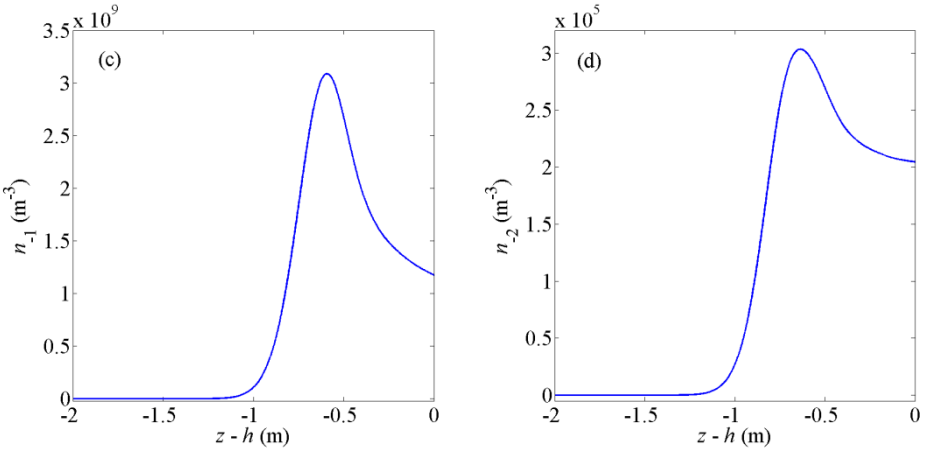

Figure 6 The number density distribution of (a) electrons, (b) ions, (c) particles carrying one negative charge, and (d) particles carrying two negative charges near the upper boundary of condensation layer at t = 1000 s.

3.3 Influence of the vertical wind speed on the spatial scale of the irregularities

The vertical wind speed is varied from 3 to 5 cm/s to investigate the influence of the wind speed on the spatial scale of the irregularities. With all other parameters remaining the same, the numerical results are shown in Fig. 7 and Fig. 8. When the wind speed is increased, the spatial scale of the irregularities increases as higher wind speed corresponds to larger critical particle radius r_c in the growth model(see Eq. (9)), which leads to longer time scale (t_c) and larger spatial scale (z_c) of ice particle growth and movement. In addition, as shown in Fig. 7(c) and (d), with the increase of wind speed, the variation amplitude of electron density and ion density near the lower boundary increases obviously. This is because the averaged radius of the ice particles increases with the extension of particle growth time (see Fig. 7(b)), and the particles' influence on the plasma increases. The variation amplitude of electron density and ion density near the upper boundary does not change notably (see Fig. 8(c) and 8(d)) because there is little variation in the averaged radii of the ice particles for different wind speed, as shown in Fig. 8(b).

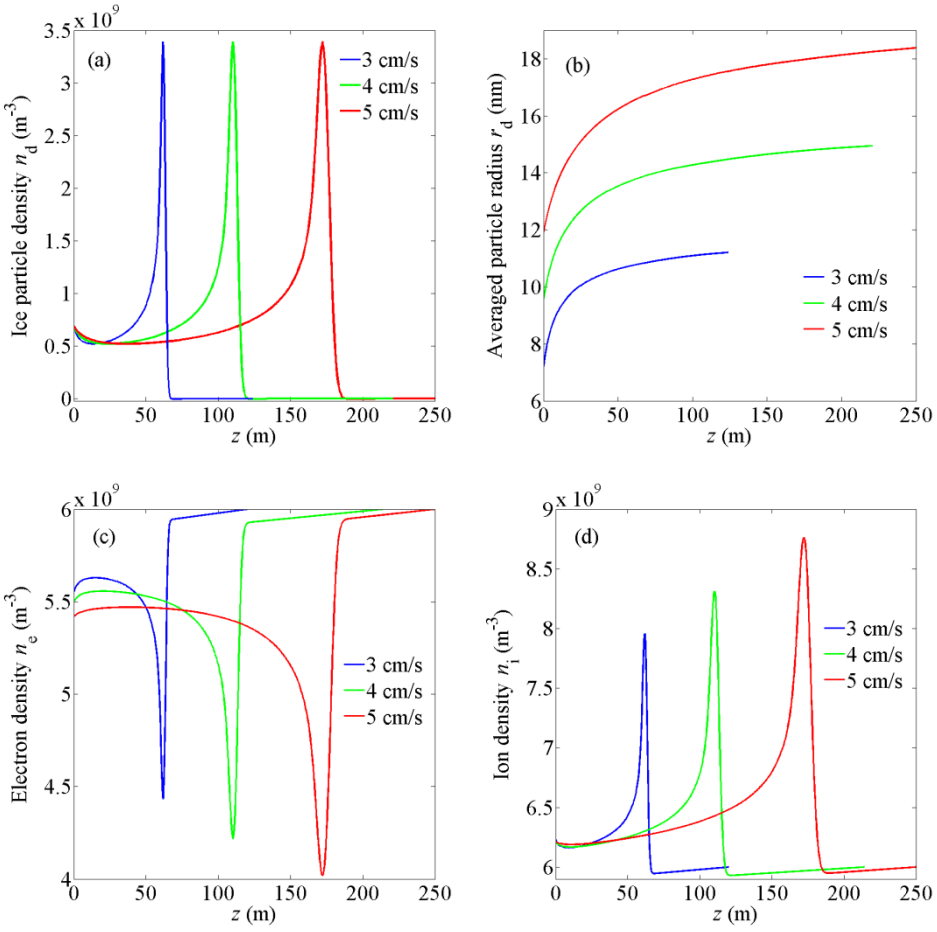

Figure 7 The distribution of (a) ice particle density, (b) the averaged particle radius, (c) electron density, and (d) ion density for various vertical wind speeds near the lower boundary of condensation layer.

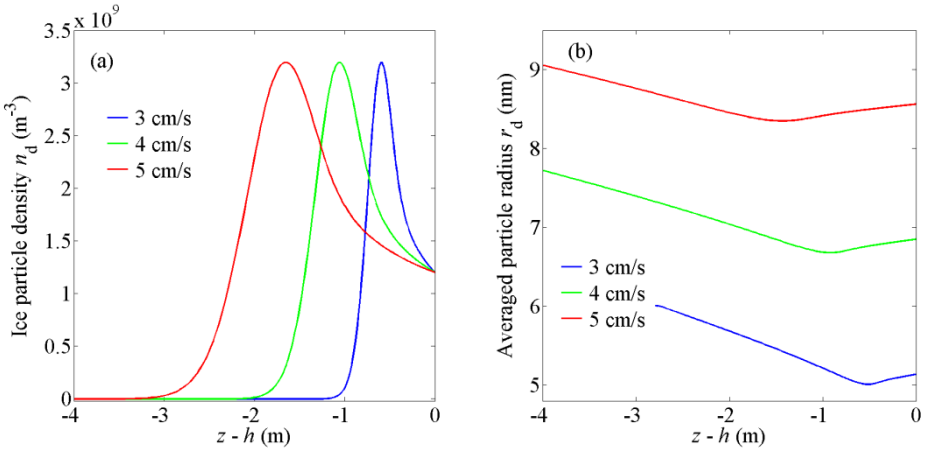

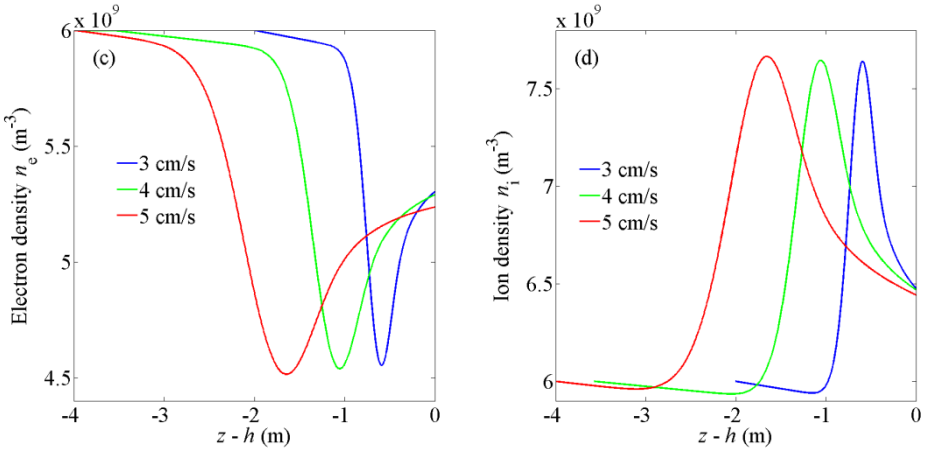

Figure 8 The distribution of (a) ice particle density, (b) the averaged particle radius, (c) electron density, and (d) ion density for various vertical wind speeds near the upper boundary of condensation layer.

3.4 Influence of the water vapor density on the spatial scale of the irregularities

Water vapor density can also affect the spatial scale of the particle density structures by modifying the change rate of particle radius. As illustrated in Fig. 9 and Fig. 10, the spatial scale of the irregularities decreases when the water vapor density increases. A lager vapor density results in a higher change rate of particle radius (see Eq. (10)) and a shorter time scale (t_c) of ice particle growth. The particles can then reach the inversion condition more quickly and the reverse position is closer to the boundary, meaning that the spatial scale of the ice particle density structures becomes shorter.

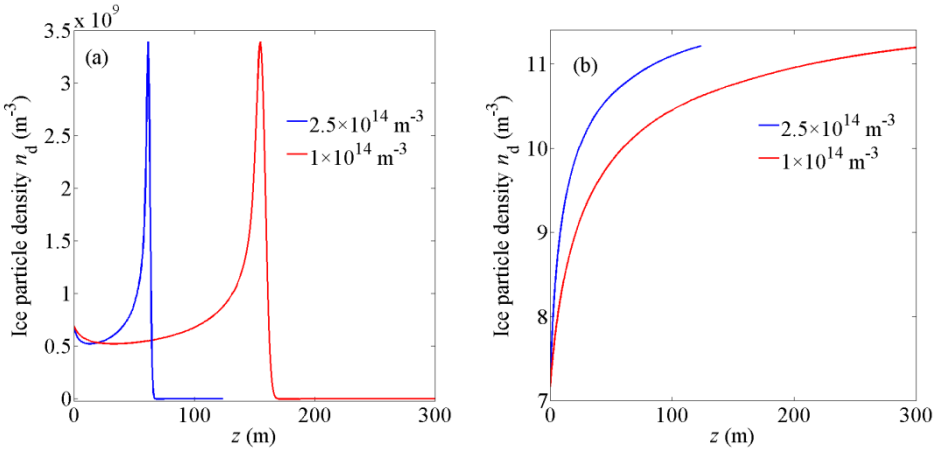

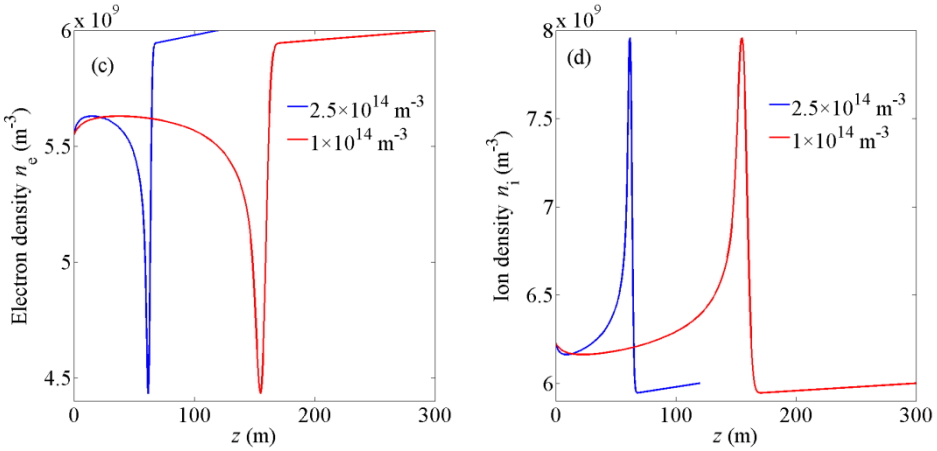

Figure 9 The distribution of (a) ice particle density, (b) the averaged particle radius, (c) electron density, and (d) ion density for various water vapor densities near the lower boundary of condensation layer.

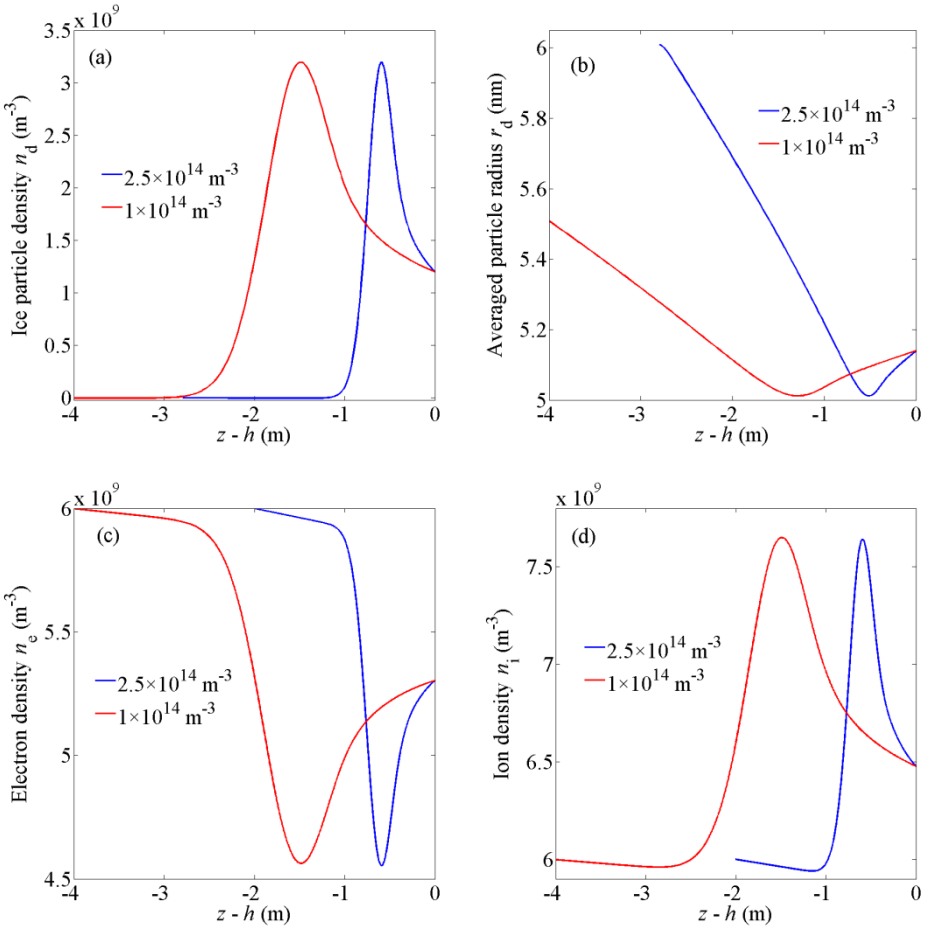

385

Figure 10 The distribution of (a) ice particle density, (b) the averaged particle radius, (c) electron density, and (d) ion density for various water vapor densities near the upper boundary of condensation layer.

3.5 Influence of the altitude on the irregularities spatial scale

The effect of the altitude on the spatial scale of the irregularities is explored in this subsection. The altitude mainly affects the neutral gas density n_n, ion composition, ion mass m_i, production rate for plasma Q, the electron-ion recombination coefficient α, and the plasma density n_0 without ice particles. In addition to 85 km, altitudes of 82 and 88 km are also included as they are near the lower and upper limits of the PMSE region (Lie‐Svendsen, et al. 2003). According to previous work (Blix 1999; Lübken 1999; Rapp and Lübken 2001), at 82 km, the positive ions are mainly $(H_3O)^+(H_2O)_3$ cluster ions with $m_i = 73\ m_u$, and other parameters are set as $n_n = 4.2 \times 10^{20}$ m^{-3}, $Q = 6.3 \times 10^7$ m^{-3}s^{-1}, $\alpha = 7 \times 10^{-12}$ m^{3}s^{-1}, and $n_0 = 3 \times 10^9$ m^{-3}. At 88 km altitude, the positive ions are mainly NO^+ with $m_i = 30\ m_u$, and other parameters are $n_n = 1.1 \times 10^{20}$ m^{-3}, $Q = 6 \times 10^7$ m^{-3}s^{-1}, $\alpha = 6 \times 10^{-13}$ m^{3}s^{-1}, and $n_0 = 1 \times 10^{10}$ m^{-3}. The numerical results are provided in Fig. 11 and Fig. 12. As the ambient plasma density n_0 varies dramatically at different altitudes, the electron density relative change $\Delta n_e/n_e$ and the ion density relative change $\Delta n_i/n_i$ are calculated for comparison, where $\Delta n_e = n_e - n_0$ and $\Delta n_i = n_i - n_0$. Figure 11(a) and Fig. 12(a) show that with the increase in altitude, the spatial scale of the ice particle density irregularities becomes shorter. The reason for this finding is that higher altitude corresponds to smaller neutral density n_n and critical particle radius r_c (see Eq. (9)), which leads to shorter time scale (t_c) and spatial scale (z_c) of ice particle growth and movement. It is notable that the spatial scale of the electron density irregularities at lower altitude is longer than that at higher altitude (see Fig. 11(c) and Fig. 12(c)). This result is consistent with the explanation provided by Bremer et al. that at lower altitude the PMSE signals detected by long-wavelength radar (half wavelength = 54 m) are stronger than those detected by short-wavelength radar (half wavelength = 2.8 m) (Bremer, et al. 1997). In addition, with the increase of altitude, the relative change amplitude of electron density and ion density decreases significantly because the averaged radius of the ice particles at higher altitude is smaller and the influence of ice particles on plasma decreases.

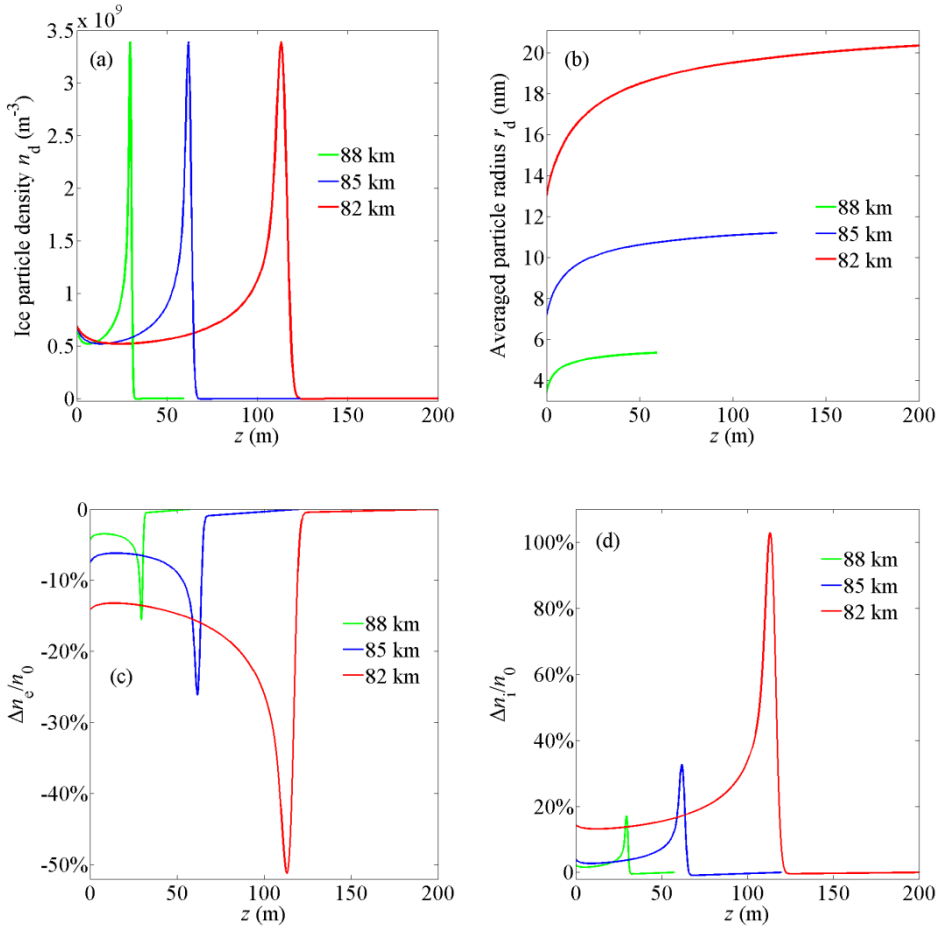

Figure 11 The distribution of (a) ice particle density, (b) the averaged particle radius, (c) the relative change of electron density $\Delta n_e/n_e$, and (d) the relative change of ion density $\Delta n_i/n_i$ at various altitudes near the lower boundary of condensation layer.

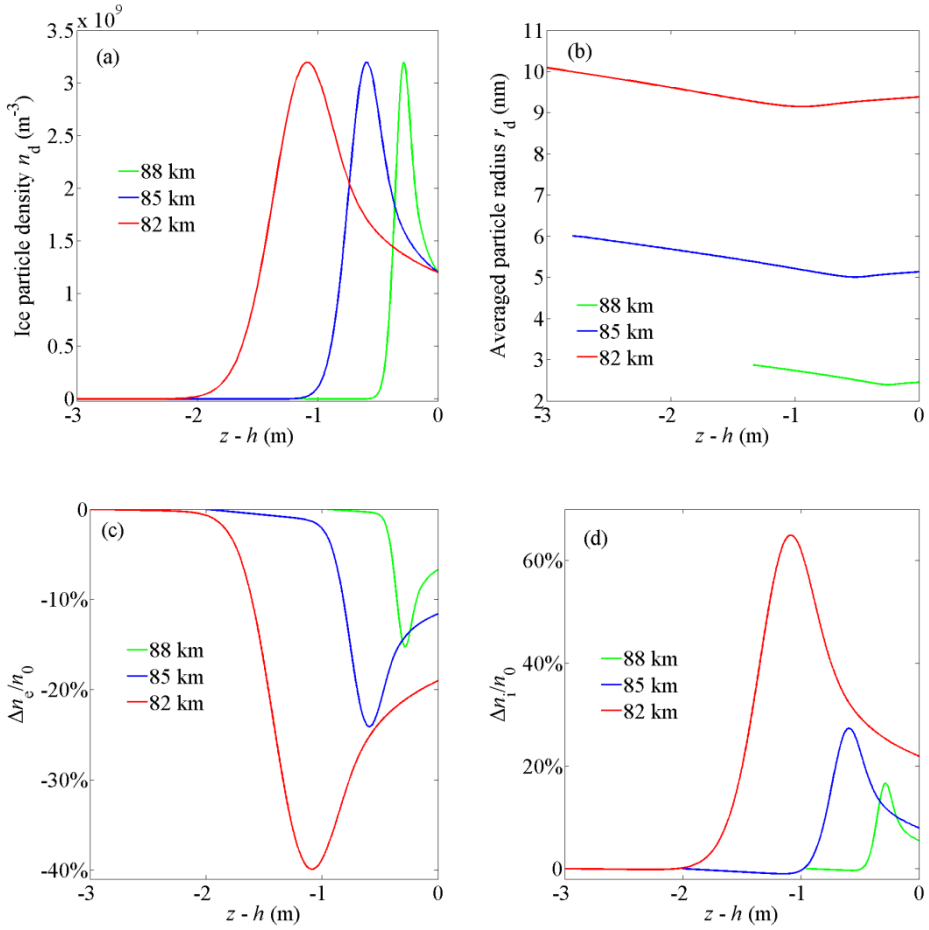

Figure 12 The distribution of (a) ice particle density, (b) the averaged particle radius, (c) the relative change of electron density $\Delta n_e/n_e$, and (d) the relative change of ion density $\Delta n_i/n_i$ at various altitudes near the upper boundary of condensation layer.

4 Conclusions

In this paper, a growth and motion model of ice particles was developed based on the equation of variable mass object motion in order to explain the formation of ice particle density irregularities with meter scale in the polar mesopause region. The density profile of ice particles with height was investigated according to the conservation of particle number. Based on the growth and motion model, small-scale structures of ice particle density were produced successfully. The density distributions of electrons and ions corresponding to the ice particle density distribution were then obtained based on quasi-neutrality and the discrete charging model. The findings are summarized as follows.

The ice particle radius increases linearly with time. However, a complex relation occurs between the velocity and radius of particles due to the variable mass of ice particles and the complicated force operating on them. For a certain radius of the condensation nucleus, ice particles can bounce near the boundary layer, which leads to a local gathering phenomenon of ice particles and the creation of meter scale ice particle density structures. The spatial scale of the density structures can be affected by vertical wind speed, water vapor density, and altitude. The spatial scale increases with the increase of wind speed, and decreases with the increase of water vapor density and altitude. Small-scale ice particle density irregularities can remain stable if these atmospheric conditions do not change. In the ice particle gathering region, the electron density is anti-correlated to the charged ice particle density and the ion density because of the plasma attachment by ice particles and plasma diffusion. To summarize, small-scale ice particle density irregularities are formed and maintained in the polar mesopause region based on the growth and motion model, and the corresponding small-scale electron density structures are in accordance with most rocket observations.

Acknowledgements

The research has been financially supported by the National Natural Science Foundation of China under Grant Nos. 11775062 and 61601419 and the Key Laboratory Foundation of National Key Laboratory of Electromagnetic Environment under Grant No. 614240319010303.

REFERENCE

Bardeen C., Toon O., Jensen E., etc.: Numerical simulations of the three‐dimensional distribution of meteoric dust in the mesosphere and upper stratosphere, Journal of Geophysical Research: Atmospheres, 113, D17202, 2008.

Blix T.: Small scale plasma and charged aerosol variations and their importance for polar mesosphere summer echoes, Advances in Space Research, 24, 537-546, 1999.

Bremer J., Hoffmann P., Manson A., etc. PMSE observations at three different frequencies in northern Europe during summer 1994[A], In Annales Geophysicae[C], 1997; pp 1317-1327.

Chen C., Scales W.: Electron temperature enhancement effects on plasma irregularities associated with charged dust in the Earth's mesosphere, Journal of Geophysical Research: Space Physics, 110, 2005.

Garcia R. R., Solomon S.: The effect of breaking gravity waves on the dynamics and chemical composition of the mesosphere and lower thermosphere, Journal of Geophysical Research: Atmospheres, 90, 3850-3868, 1985.

Havnes O., Trøim J., Blix T., etc.: First detection of charged dust particles in the Earth's mesosphere, Journal of Geophysical Research: Space Physics, 101, 10839-10847, 1996.

Hill R., Bowhill S.: Collision frequencies for use in the continuum momentum equations applied to the lower ionosphere, Journal of Atmospheric and Terrestrial Physics, 39, 803-811, 1977.

Hill R., Gibson-Wilde D., Werne J., etc.: Turbulence-induced fluctuations in ionization and application to PMSE, Earth, planets and space, 51, 499-513, 1999.

Jensen E., Thomas G. E.: A growth - sedimentation model of polar mesospheric clouds: Comparison with SME measurements, Journal of Geophysical Research: Atmospheres, 93, 2461-2473, 1988.

Körner U., Sonnemann G.: Global three - dimensional modeling of the water vapor concentration of the mesosphere - mesopause region and implications with respect to the noctilucent cloud region, Journal of Geophysical Research: Atmospheres, 106, 9639-9651, 2001.

Kopnin S., Kosarev I., Popel S., etc.: Localized structures of nanosize charged dust grains in Earth's middle atmosphere, Planetary and Space Science, 52, 1187-1194, 2004.

Lübken F. J.: Thermal structure of the Arctic summer mesosphere, Journal of Geophysical Research: Atmospheres, 104, 9135-9149, 1999.

Lübken F. J., Rapp M., Blix T., etc.: Microphysical and turbulent measurements of the Schmidt number in the vicinity of polar mesosphere summer echoes, Geophysical Research Letters, 25, 893-896, 1998.

Lie - Svendsen Ø., Blix T., Hoppe U. P., etc.: Modeling the plasma response to small - scale aerosol particle perturbations in the mesopause region, Journal of Geophysical Research: Atmospheres, 108, 8442, 2003.

Lieberman M. A., Lichtenberg A. J.: Principles of plasma discharges and materials processing, John Wiley & Sons, 2005.

Mahmoudian A., Scales W.: On the signature of positively charged dust particles on plasma irregularities in the mesosphere, Journal of Atmospheric and Solar-Terrestrial Physics, 104, 260-269, 2013.

Natanson G.: On the theory of the charging of amicroscopic aerosol particles as a result of capture of gas ions, Sov. Phys. Tech. Phys., 30, 573-588, 1960.

Pfaff R., Holzworth R., Goldberg R., etc.: Rocket probe observations of electric field irregularities in the polar summer mesosphere, Geophysical research letters, 28, 1431-1434, 2001.

Röttger J., La Hoz C., Kelley M. C., etc.: The structure and dynamics of polar mesosphere summer echoes observed with the EISCAT 224 MHz radar, Geophysical research letters, 15, 1353-1356, 1988.

Röttger J., Rietveld M., La Hoz C., etc.: Polar mesosphere summer echoes observed with the EISCAT 933 - MHz radar and the CUPRI 46.9 - MHz radar, their similarity to 224 - MHz radar echoes, and their relation to turbulence and electron density profiles, Radio Science, 25, 671-687, 1990.

Rapp M., Lübken F.-J.: Modelling of particle charging in the polar summer mesosphere: Part

1—General results, Journal of Atmospheric and Solar-Terrestrial Physics, 63, 759-770, 2001.

Rapp M., Lübken F.-J.: Polar mesosphere summer echoes (PMSE): Review of observations and current understanding, Atmospheric Chemistry and Physics, 4, 2601-2633, 2004.

Rapp M., Lübken F. J.: On the nature of PMSE: Electron diffusion in the vicinity of charged particles revisited, Journal of Geophysical Research: Atmospheres, 108, 8437, 2003.

Reid G. C.: Ice particles and electron "bite-outs" at the summer polar mesopause, Journal of Geophysical Research: Atmospheres, 95, 13891-13896, 1990.

Robertson S., Sternovsky Z.: Effect of the induced-dipole force on charging rates of aerosol particles, Physics of Plasmas, 15, 040702, 2008.

Scales W., Ganguli G.: Investigation of plasma irregularity sources associated with charged dust in the Earth's mesosphere, Advances in Space Research, 34, 2402-2408, 2004.

Schunk R.: Mathematical structure of transport equations for multispecies flows, Reviews of Geophysics, 15, 429-445, 1977.

Seele C., Hartogh P.: Water vapor of the polar middle atmosphere: Annual variation and summer mesosphere conditions as observed by ground-based microwave spectroscopy, Geophysical Research Letters, 26, 1517-1520, 1999.